Check for updates

Rare-earth-doped fluoride nanoparticles with engineered long luminescence lifetime for time-gated *in vivo* optical imaging in the second biological window†

Meiling Tan,‡[a] Blanca del Rosal, [ID] ‡[b] Yuqi Zhang,[a] Emma Martín Rodríguez, [ID] *[d,g]
Jie Hu,[c,d] Zhigang Zhou,[e] Rongwei Fan,[e] Dirk H. Ortgies, [ID] [c,d] Nuria Fernández,[f]
Irene Chaves-Coira,[h] Ángel Núñez,[h] Daniel Jaque [ID] [c,d] and Guanying Chen [ID] *[a]

Biomedicine is continuously demanding new luminescent materials to be used as optical probes for the acquisition of high resolution, high contrast and high penetration *in vivo* images. These materials, in combination with advanced techniques, could constitute the first step towards new diagnosis and therapy tools. In this work, we report on the synthesis of long lifetime rare-earth-doped fluoride nanoparticles by adopting different strategies: core/shell and dopant engineering. The here developed nanoparticles show intense infrared emission in the second biological window with a long luminescence lifetime close to 1 millisecond. These two properties make the here presented nanoparticles excellent candidates for time-gated infrared optical bioimaging. Indeed, their potential application as optical imaging contrast agents for autofluorescence-free *in vivo* small animal imaging has been demonstrated, allowing high contrast real-time tracking of gastrointestinal absorption of nanoparticles and transcranial imaging of intracerebrally injected nanoparticles in the murine brain.

1. Introduction

Fluorescence-based optical imaging utilizes color-encoded emissions (typically in the visible range) from endogenous or exogenous fluorophores to acquire detailed images of organs and tissues as well as subcellular structures to unravel biologi-

[a] *MIIT Key Laboratory of Critical Materials Technology for New Energy Conversion and Storage, School of Chemistry and Chemical Engineering & Key Laboratory of Micro-systems and Micro-structures, Ministry of Education, Harbin Institute of Technology, 150001 Harbin, People's Republic of China.*
E-mail: chenguanying@hit.edu.cn
[b] *Centre for Micro-Photonics, Faculty of Science, Engineering and Technology, Swinburne University of Technology, PO Box 218, Hawthorn, VIC 3122, Australia*
[c] *Departamento de Física de Materiales, Universidad Autónoma de Madrid, Madrid 28049, Spain. E-mail: emma.martin@uam.es*
[d] *Instituto Ramón y Cajal de Investigación Sanitaria, IRYCIS, Ctra. Colmenar km. 9.100, Madrid 28034, Spain*
[e] *National Key Laboratory of Tunable Lasers, Institute of Optical-Electronics, Harbin Institute of Technology, 150001 Harbin, People's Republic of China*
[f] *Departamento de Fisiología, Facultad de Medicina, Avda. Arzobispo Morcillo 2, Universidad Autónoma de Madrid, 28029 Madrid, Spain*
[g] *Departamento de Física Aplicada, Universidad Autónoma de Madrid, Madrid 28049, Spain. E-mail: emma.martin@uam.es*
[h] *Departamento de Anatomía, Histología y Neurociencia, Facultad de Medicina, Universidad Autónoma de Madrid, Madrid, Spain*
† Electronic supplementary information (ESI) available. See DOI: 10.1039/c8nr02382d
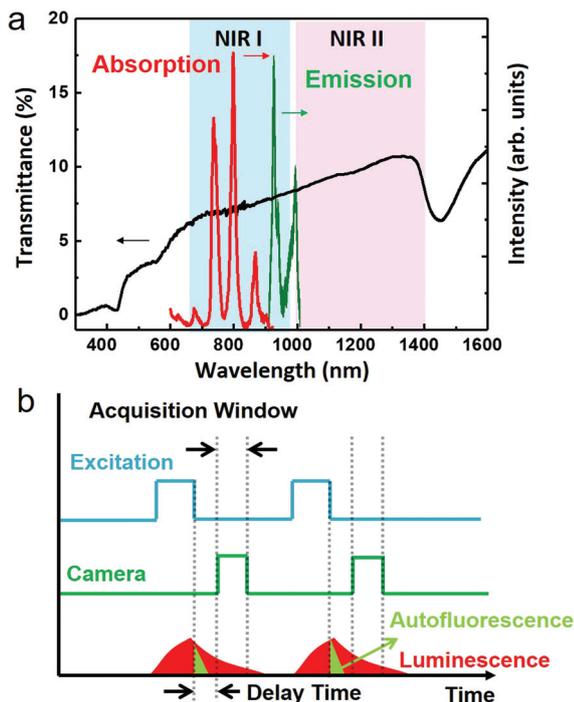‡ These authors contributed equally to this work.

cal complexities.[1] This technique is non-invasive and non-ionizing, and allows video-rate imaging with high spatial resolutions not only at the optical microscopy level (sub-micrometre, *ca*. 250 nm), but also at the optical diffraction-limited level (optical super-resolution, *ca*. 20 nm).[1–5] As a result, fluorescence imaging is applied in a plethora of fields ranging from pre-clinical testing and clinical diagnosis, to precise image-guided surgical excision of tumors, and to molecular-level monitoring of disease progression.[6–12] However, fluorescence imaging has been limited by the low penetration depth of light into tissues (<1 mm for wavelengths in the visible range of 400–650 nm) and by the autofluorescence of biological tissues.[13,14] These two problems result in the loss of spatial resolution and the decrease of the signal to noise ratio, and thus in a serious deterioration of the acquired *in vivo* images. The problem of penetration has been alleviated in the past years, as it has been shown that centimeter-scale imaging depths can be accomplished when shifting both fluorescence and excitation wavelengths from the visible to the near infrared (NIR) optical biological windows, where the absorption of tissues reaches a minimum. The NIR region of 650–950 nm is known as the first biological window (NIR I), while the NIR region of 1000–1350 nm is known as the second biological window (NIR II) (Fig. 1a). Recent experimental results have demonstrated that using fluorescent labels emitting in NIR II

Fig. 1 a. Schematic illustration of the first (NIR I) and second (NIR II) biological windows. The black curve represents the transmission of light through a nude mouse skin (thickness of 1 mm). The absorption and emission spectra of our synthesized $NaYF_4:Yb^{3+},Nd^{3+}@CaF_2$ NPs are also included in this figure for reference. b. A schematic depiction of the general principle of time-gated optical imaging. Periodic excitation is usually triggered by high repetition pulsed lasers. Image acquisition triggered a determined delay time after the end of each laser pulse.

instead of NIR I result in an improved contrast and imaging depth due to the reduction of light scattering,[15,16] which scales as $\lambda^{-\alpha}$, where λ is the wavelength and α has a value from 0.2 to 4 depending on the composition of the tissue.[17] Therefore, a range of fluorescent materials with excitation in NIR I and emission in NIR II have been developed and tested for small animal imaging. These materials span from small organic NIR fluorescent dyes to inorganic nanoparticles (NPs), such as carbon nanotubes,[18] rare earth doped nanocrystals,[19] and NIR quantum dots[20–22] (among them, Ag_2S quantum dots can be highlighted),[23,24] enabling through-skull fluorescence imaging of the murine brain with sub-10 µm resolution.[16] Yet, even in NIR II, infrared-excited autofluorescence from tissues remains substantial, as some biological components show non-negligible emissions beyond 1000 nm, resulting in a dramatic reduction of the image contrast.[13] Optical probes with longer emission wavelengths (>1300 nm) can help improve the contrast by minimizing spectral overlap with autofluorescence; however, such probes remained rare.

Time-gated optical imaging is an established stroboscopic technique, which can eliminate the nuisance of autofluorescence by exploiting the long lifetime of emissions from optical probes (~µs–ms) against the short lifetime (~ns) of tissue autofluorescence.[25–28] Despite their spectral overlap, the differ-

ence of emission profiles in the time domain allows a straightforward removal of the autofluorescence background by capturing images in a time window that excludes the unwanted natural emissions from tissue endogenous luminophores (Fig. 1b).[28,29] This technique employs periodic laser pulses to perform light excitation, while the excitation train of pulses is synchronized, but with a precisely defined time delay (longer than the lifetime of the autofluorescence), with the activation of the camera. It has been shown that time-gated imaging, with long lifetime lanthanide complexes (typically containing europium or terbium), can allow high contrast fluorescence microscopy imaging of cells in the visible range.[30] Moreover, in combination with the long emission lifetime (5–13 µs) of porous silicon nanoparticles, time-gated optical imaging enables a >20-fold improvement of the signal to background contrast ratio *in vivo* when imaging with photoluminescence (600–900 nm) in the NIR I window.[29,31] Despite these advantages, the use of time-gated techniques for *in vivo* optical imaging in the NIR II window remains elusive, because most NIR II luminophores have emission lifetimes commensurate with that of autofluorescence, significantly limiting their usefulness in this regard.

Lanthanide-based luminescent nanomaterials constitute an emerging class of promising biolabels for *in vivo* time-gated optical imaging in NIR II. This is because lanthanide ions have not only abundant energy levels in the infrared range, but also typically long emission lifetimes (on the order of 10^{-4}–10^{-3} s).[32,33] Moreover, their advantages of characteristic narrow excitation and emission bands, absence of photobleaching, and no known significant toxic effects neither in *in vivo* nor in *in vitro*, make them perfect as biolabels for optical bioimaging in the time domain.[28] Though particles doped with infrared-emitting lanthanide ions (such as neodymium, Nd^{3+}, or erbium, Er^{3+}) have been reported for steadystate *in vivo* imaging in the NIR II window, the advantages of NIR II lanthanide-doped particles with a tailored long lifetime emission for time domain imaging have not yet been revealed.[34–41] Recently, we demonstrated in a proof-of-concept that $NaGdF_4:Nd^{3+}$ particles with a size of 600–800 nm could enable time-gated optical imaging of mice at 1050 nm, entailing a remarkable improvement in the contrast of fluorescence images due to the removal of autofluorescence.[37] However, to reach sufficiently long lifetimes (200 µs) and efficient luminescence, micrometer-scale particle size had to be employed, which is too large for many bioapplications. It is, therefore, important to develop small-sized lanthanide-doped nanocrystals with tailored long lifetime luminescence for time-gated optical imaging in the NIR II window.

By examining the energy level structures of lanthanide ions, we found that ytterbium (Yb^{3+}) ions possess a unique structure and have only one single excited state ($^2F_{5/2}$), which produces an emission centered at 1000 nm (the $^2F_{7/2} \rightarrow ^2F_{5/2}$ transition) lying right across the NIR I and NIR II windows (Fig. 1a).[42,43] Moreover, the incorporation of Yb^{3+} ions in crystallized materials typically results in emission lifetimes of hundreds of microseconds, several orders of magnitudes above the

autofluorescence lifetime.[44] Both features make Yb^{3+} ion-containing nanocrystals attractive for NIR II time-gated optical imaging. Note that Yb^{3+} ions are commonly used as sensitizers for many activators (Er^{3+}, Ho^{3+}, Tm^{3+}, *etc.*) in doped NPs to produce intense photon upconversion.[42,45] In fact, they do have excellent radiative properties to be utilized as emitters, as many types of commercial lasers have employed Yb^{3+} ions to realize a tunable wavelength lasing output at ~1000 nm.[46,47] However, to excite Yb^{3+} ion emitters, a laser output with a wavelength at ~980 nm has to be used, which, unfortunately, overlaps largely with the absorption peak of water molecules that are dominant in biological samples. Overexposure of biological species to 980 nm light would cause overheating issues, resulting in significant cell death and tissue damage.[43,48–51] This problem can be addressed by co-doping NPs with neodymium (Nd^{3+}) ions, which act as sensitizers for Yb^{3+} ions (Fig. 2a) and have an intense absorption band at around 800 nm where water molecules and biological tissues have an about 10 times lower absorption coefficient. As a result, we reason that small-sized Nd^{3+}/Yb^{3+} co-doped NPs with engineered bright and long lifetime luminescence at 1000 nm hold promise for employment as fluorescent biolabels for *in vivo* time-gated optical imaging in the NIR II window.

In this work, we report on two approaches to produce a class of sub-15 nm Nd/Yb-codoped luminescent NPs with enhanced emission efficiency and long lifetime, allowing high contrast time-gated *in vivo* imaging in the NIR II window. The first one is to incorporate thulium (Tm^{3+}) dopants in Yb^{3+}/Nd^{3+} codoped fluoride NPs (~13 nm) devoid of shell protec-

tion, while the second one is to utilize a core/shell structure to produce enhanced and long lifetime emissions from $NaYF_4$: Yb^{3+},Nd^{3+}@CaF_2 core/shell NPs (~9 nm). For the first case, we compared the effect of Tm^{3+} doping in two fluoride hosts ($NaGdF_4$ and $NaDyF_4$) and observed that the presence of Gd^{3+} in the host crystal gives NPs with a lifetime longer than 1 millisecond. In the second case, we performed a systematic optimization of doping concentrations of both Nd^{3+} and Yb^{3+} ions in the $NaYF_4$ core, which enabled enhancing the absorption of excitation light at 800 nm while shortening the distance between Nd^{3+} and Yb^{3+} for an improved energy transfer efficiency. Coating with an inert biocompatible CaF_2 shell served the purpose of reducing surface-related quenching, thereby increasing the luminescence intensity at 1000 nm by about 45 times and lifetime from about 50 to 830 μs. The suitability of the NPs developed in both approaches for *in vivo* time-gated optical imaging in the NIR II window has been demonstrated, showing superior performance to that of commercially available Ag_2S NPs.

2. Experimental

All synthesis, characterization, and imaging details are described in detail in the ESI.† All *in vivo* experiments carried out in this work were approved by the Ethics Committee from Universidad Autónoma of Madrid (CEIT) in the frame of the project MAT2010-21270-C04-01 supported by the Spanish Ministerio de Economía y Competitividad.
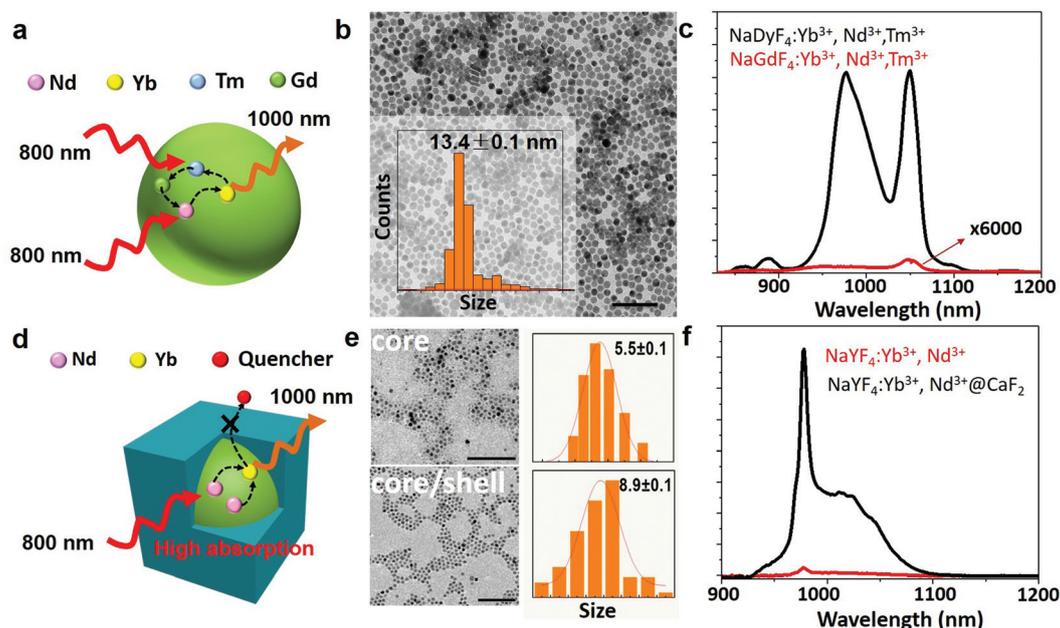

Fig. 2 a. Schematic illustration of energy transfer in the $NaGdF_4$:2% Yb,3% Nd,0.2% Tm NPs; b. TEM image of the $NaGdF_4$:2% Yb,3% Nd,0.2% Tm NPs (scale bar, 100 nm), with their size distribution shown in the inset; c. emission spectra from the $NaGdF_4$:2% Yb,3% Nd,0.2% Tm NPs and the $NaDyF_4$:2% Yb,3% Nd,0.2% Tm NPs in hexane under excitation at 790 nm; d. schematic illustration of the core/shell structure designed to suppress the surface quenching effect; e. TEM image of the core $NaYF_4$:10% Yb^{3+},30% Nd^{3+} and core/shell $NaYF_4$:10% Yb^{3+},30% Nd^{3+}@CaF_2 NPs (scale bar, 100 nm), with their size distribution shown (right); and f. emission spectra from the core and the core/shell NPs dispersed in hexane under excitation at 800 nm.

3. Results and discussion

We first explored the possibility of obtaining long luminescence-lifetime NPs in single core NPs. We selected $NaGdF_4$:2% Yb^{3+},3% Nd^{3+},0.2% Tm^{3+} NPs, due to their good luminescence properties already reported.[52] The synthesis procedure of $NaGdF_4$:2% Yb^{3+},3% Nd^{3+},0.2% Tm^{3+} NPs is described in the ESI.† The host materials and dopants that enhance the energy transfer process can lead to an intense and long lifetime Yb^{3+} emission. The mechanism is represented schematically in Fig. 2a and in detail in Fig. S1.† The co-doped Nd^{3+} and Tm^{3+} ions, which increase the absorption at 800 nm, and Gd^{3+} acted as the energy bridge for the energy transfer from Tm^{3+} to Nd^{3+}, enhancing the emission of Yb^{3+} under 800 nm excitation. The size of $NaGdF_4$:2% Yb^{3+},3% Nd^{3+},0.2% Tm^{3+} NPs was found to be approximately 13 nm, according to the transmission electron microscopy (TEM) image and size distribution shown in Fig. 2b. For comparison, $NaDyF_4$:2% Yb^{3+},3% Nd^{3+},0.2% Tm^{3+} NPs were also synthesized, to study the role of Gd^{3+} in the $Nd^{3+} \rightarrow Yb^{3+}$ energy transfer process. Fig. 2c shows the emission spectra of $NaGdF_4$:2% Yb^{3+},3% Nd^{3+},0.2% Tm^{3+} and $NaDyF_4$:2% Yb^{3+},3% Nd^{3+},0.2% Tm^{3+} NPs under 790 nm excitation under the same experimental conditions. The $NaGdF_4$:2% Yb^{3+},3% Nd^{3+},0.2% Tm^{3+} NPs show two intense emission bands in the region from 850 nm to 1100 nm, the first one at 980 nm, corresponding to the $^2F_{7/2} \rightarrow {}^2F_{5/2}$ transition of Yb^{3+}; and the second one at 1060 nm corresponding to the $^4F_{3/2} \rightarrow {}^4I_{11/2}$ transition of Nd^{3+}. In comparison, the $NaDyF_4$:2% Yb^{3+},3% Nd^{3+},0.2% Tm^{3+} sample shows an emission intensity about 6×10^4 times weaker. It is also remarkable that the spectrum is dominated by the 1060 nm band from Nd^{3+}, demonstrating the importance of Gd^{3+} in the energy transfer processes that leads to the Yb^{3+} emission. Dispersibility in water was achieved by coating the $NaGdF_4$:2% Yb^{3+},3% Nd^{3+},0.2% Tm^{3+} and $NaDyF_4$:2% Yb^{3+},3% Nd^{3+},0.2% Tm^{3+} NPs with a PEGylated lipid (DSPE-PEG-amine). But due to the existence of surface-related quenching effects, the single core $NaGdF_4$:2% Yb^{3+},3% Nd^{3+},0.2% Tm^{3+} NPs cannot support the high doping concentration of lanthanides to further enhance the absorption of excitation light at 800 nm and increase the number of emitters for higher luminescence intensity. Recent results show that a core/shell structure is able to prevent the migration process of excited energy from lanthanide dopants to surface quenching sites, which mediates in part the lanthanide cross relaxation induced concentration quenching effect.[53] As a result, a core/ shell structure is crucial for high lanthanide doped NPs, along with the suppression of surface-related quenching.

In the case of the core/shell NPs, $NaYF_4$:Yb^{3+},Nd^{3+} NPs were used as seeds for the epitaxial growth of an inert calcium fluoride (CaF_2) shell (Fig. 2d). CaF_2 was chosen as the shell layer because it has a low lattice mismatch with the core, broad spectral range of optical transparency and high stability in aqueous environments; additionally, because its constituents (calcium and fluoride ions) are common components of biological tissues, which can enhance the biocompatibility of the

resulting core/shell NPs.[54] Both the $NaYF_4$:Yb^{3+},Nd^{3+} core and the $NaYF_4$:Yb^{3+},Nd^{3+}@CaF_2 core/shell NPs doped with varied concentrations of Yb^{3+} and Nd^{3+} were synthesized *via* the thermal decomposition of metallic trifluoroacetates at high temperatures (see the ESI†). The TEM image of the synthesized core $NaYF_4$:Yb^{3+},Nd^{3+} NPs reveals a spherical shape with an average diameter of about 5.5 nm (Fig. 2e). The obtained core/ shell NPs are monodisperse with a uniform, cubic shape, having an average size close to 9 nm. The X-ray diffraction (XRD) patterns indicate that both the core and the core/shell structures are of the cubic crystallographic phase (Fig. S2†). All the XRD peaks are consistent with the standard patterns of α-$NaYF_4$ (JCPDS No. 77-2042) and CaF_2 (JCPDS No. 77-2096). Energy-dispersive X-ray (EDX) spectra confirm the presence of Ca in the core/shell structure, suggesting the successful preparation of the designated $NaYF_4$:Yb^{3+},Nd^{3+}@CaF_2 core/shell NPs (Fig. S3†).

The absorption spectrum of the core/shell NPs (Fig. S4†) displays the characteristic absorption bands of Nd^{3+} ions (at 890, 800 and 750 nm) and the absorption band of Yb^{3+} ions (centered at around 980 nm). The photoluminescence spectra of the core and core/shell NPs, obtained under optical excitation at 800 nm, are included in Fig. 2f. The emission spectra show two emission peaks (*ca.* 1000 nm), centered at 980 and 1011 nm, both of which arise from radiative transitions between Stark energy sublevels of the excited ($^2F_{5/2}$) and ground states ($^2F_{7/2}$) of Yb^{3+} ions. No luminescence from Nd^{3+} ions was observed in those NPs doped with a high lanthanide concentration. Note that the excitation spectrum of the core/ shell NPs presents three emission peaks centered at 750, 800 and 860 nm, which matches well with the absorption peaks of Nd^{3+} ions (Fig. S4†). This spectral match unequivocally demonstrates the possibility of $Nd^{3+} \rightarrow Yb^{3+}$ energy transfer processes, thus enabling the excitation of core/shell NPs through Nd^{3+} absorption in the NIR I window (Fig. 2f).[55,56] Fig. 2f also includes the emission spectrum from the corresponding core NPs. It is evidenced that the addition of an inert CaF_2 shell results in a 45 times increase in the emission intensity. This can be attributed to the reduction of surface lattice defects of the core nanocrystals that act as luminescence quenchers, as well as to the decrease of nonradiative interactions between surface lanthanide ions and luminescence quenchers from the surrounding environment (solvents, ligands, *etc.*), created by the spatial isolation of the epitaxial shell (Fig. 2d).[57,58]

To probe the impact of the absorption-enhanced fluorescence and to optimize the energy transfer between Nd^{3+} and Yb^{3+} ions, we investigated the concentration effect of sensitizer Nd^{3+} ions on the overall emission intensity of the core/ shell structure. For this purpose, we prepared a set of α-$NaYF_4$:10% Yb^{3+},x% Nd^{3+} core NPs doped with different Nd^{3+} contents (x = 10, 20, 40, 60), and then utilized the same amount of the CaF_2 shell precursor for coating. All synthesized core and core/shell NPs present virtually identical sizes, as shown by the TEM images and size distribution (Fig. S5†). Increasing the Nd^{3+} doping concentration from 10% to 30% results in a relevant increase in the fluorescence emission

intensity. However, a decrease in the emission intensity is observed if the Nd^{3+} doping level is further increased (50% and 80%) (Fig. S6†). No significant changes in the shape of the emission spectrum were observed, revealing a minimum distortion of the crystalline field of the host lattice ($NaYF_4$) even at high dopant concentrations of Nd^{3+} ions. Whereas the absorption of the excitation light can be enhanced by increasing the Nd^{3+} doping concentration, the deleterious cross-relaxation processes between Nd^{3+} ions are simultaneously activated, which results in a reduced energy transfer to Yb^{3+} ions. The final emitted intensity generated by Yb^{3+} ions would result from the balance between these two effects, indicating an optimized Nd^{3+} concentration of 30%.

We next verified the role of the concentration of the activator Yb^{3+} ions in the overall energy transfer process by evaluating the emission intensity as a function of Yb^{3+} concentration in the range from 10% to 60%. As occurred when changing the concentration of Nd^{3+} ions, no effects on the morphology and size of the NPs were observed (Fig. S7†). Increasing the Yb^{3+} concentration resulted in a progressive reduction in the emission intensity (Fig. S8†). This result indicates that a long Yb^{3+}–Yb^{3+} interionic distance is essential for efficient energy transfer from Nd^{3+} to Yb^{3+} ions. This has been explained in the past in terms of the activation of an $Yb^{3+} \rightarrow Nd^{3+}$ back energy transfer process that could occur for high Yb^{3+} concentrations (note that in a back transfer process, the Yb^{3+} ion acts as a sensitizer).[59] Additionally, the reduction of ytterbium emission at high doping levels could also be due to the activation of concentration quenching effects as described in the literature.[60] The optimal doping levels for Yb^{3+} and Nd^{3+} in the $NaYF_4$:Yb^{3+},Nd^{3+}@CaF_2 core/shell NPs were determined to be 10% and 30%, respectively.

Finally, to verify that the co-doping approach (simultaneous incorporation of both Nd^{3+} and Yb^{3+} in the core) was the best choice for optimizing the energy transfer rate from Nd^{3+} to Yb^{3+}, we evaluated the energy transfer process when the sensitizer and activator ions are spatially separated in the core/shell structure. In particular, we prepared the $NaYF_4$:10% Yb^{3+}@CaF_2:30% Nd^{3+} core/shell structure, and compared the NIR II emission at 1000 nm with that from single-core co-doped $NaYF_4$:10% Yb^{3+},30% Nd^{3+}@CaF_2 core/shell NPs. We observed that the separation of Nd^{3+} and Yb^{3+} ions in the core/shell structure lets the emission peak at 860 nm from Nd^{3+} ions dominate over the emission peak at 1000 nm from Yb^{3+} ions, as opposed to the result achieved with the co-doping approach. Moreover, the interesting NIR II emission at 1000 nm is about 10 times weaker than that of the co-doped $NaYF_4$:10% Yb^{3+}@CaF_2:30% Nd^{3+} core/shell NPs (Fig. S9†). This result confirms the importance of positioning both Nd^{3+} and Yb^{3+} ions in the core of a core/shell structure to produce a strong NIR emission at 1000 nm.

Prior to their application in time-gated *in vivo* imaging experiments, the optimal core/shell NPs ($NaYF_4$:10% Yb^{3+},30% Nd^{3+}@CaF_2) were provided with dispersibility in aqueous media by replacing the oleate molecules present on the surface of the NPs with poly(acrylic acid) (PAA, MW = 18 000). The pro-

cedure is described in detail in the ESI.† The Fourier transform infrared (FTIR) spectra of the as-synthesized and modified NPs (Fig. S10†) showed an increased intensity of the band at 1724 cm^{-1} (that can be assigned to –C=O groups) demonstrating that a large amount of COOH groups had been added to the core/shell NP surface. This is further supported by the increased intensity of the band at 3454 cm^{-1} (3100–3600 cm^{-1}, OH groups), and the decreased intensity of the band at 2927 cm^{-1} (CH_3 groups). This indicates a successful replacement of the original oleic acid ligand by PAA. In addition, the hydrodynamic size of the PAA-coated core/shell NPs was evaluated to be about 37 nm using dynamic light scattering (DLS) (Fig. S11†), much larger than the size shown in the TEM (~9 nm) image. This larger size can be attributed to the presence of PAA in contact with the aqueous environment, evidencing the successful ligand transfer, and demonstrating that, even after the ligand transfer, the NPs are small enough for biological applications. The emission intensity from the water-dispersible core/shell NPs was about two times lower than that from the hexane-dispersed form (Fig. S12†), which could be attributed to the imperfectness of the shell and the existence of a large amount of –OH groups (a high phonon energy of ~3500 cm^{-1}) in water, resulting in the non-radiative depopulation of the $^2F_{5/2}$ state of Yb^{3+} ions.[61] The cytotoxicity of the NPs was evaluated *via* a methyl thiazolyl tetrazolium (MTT) assay on HeLa cells, which indicated no significant effects of the NPs on cell viability (Fig. S13†).

To evaluate the suitability of the NPs for time-gated imaging in the second biological window, the decay curve of the NIR II emission at 1000 nm (corresponding to the $^2F_{5/2} \rightarrow {}^2F_{7/2}$ transition of Yb^{3+} ions) from both types of NPs was acquired (Fig. 3). The decay curve could be fitted to a single exponential giving a value of $\tau = (1350 \pm 50)$ μs for the $NaGdF_4$:2% Yb^{3+},3% Nd^{3+},0.2% Tm^{3+} NPs (Fig. 3a). This extremely long lifetime makes these particles an ideal fluorophore for time-gated imaging, as the detection can be delayed without observing a decrease in the emitted intensity from the NPs (for a delay of 1 μs the remaining signal will be 99.93% of the original signal). In good agreement with the observed emitted intensity, the lifetime of the $NaDyF_4$:2% Yb^{3+},3% Nd^{3+},0.2% Tm^{3+} NPs was $\tau = (55 \pm 5)$ μs (Fig. 3a), supporting once more the importance of Gd^{3+} in the emission mechanism of Yb^{3+}. For the PAA-coated $NaYF_4$:10% Yb^{3+},30% Nd^{3+} and $NaYF_4$:10% Yb^{3+},30% Nd^{3+}@CaF_2 NPs, whereas only core NPs presented a lifetime of 51 μs for Yb^{3+} ions, the lifetime of the core/shell NPs in aqueous dispersion was determined to be as long as 833 μs, indicating their suitability for time-gated imaging (Fig. 3b). Note that the significant difference of the lifetime for the $NaGdF_4$:2% Yb^{3+},3% Nd^{3+},0.2% Tm^{3+} and $NaYF_4$:10% Yb^{3+},30% Nd^{3+} core NPs is due to both particles having a distinct concentration of lanthanide dopants. We also compared the emission intensity of the core/shell NPs developed in this work with that of commercial Ag_2S NPs, whose emission band lies at around 1230 nm (Fig. S14†), and which constitute one of the few probes available for high contrast imaging in the second biological window.[62,63] For an equi-
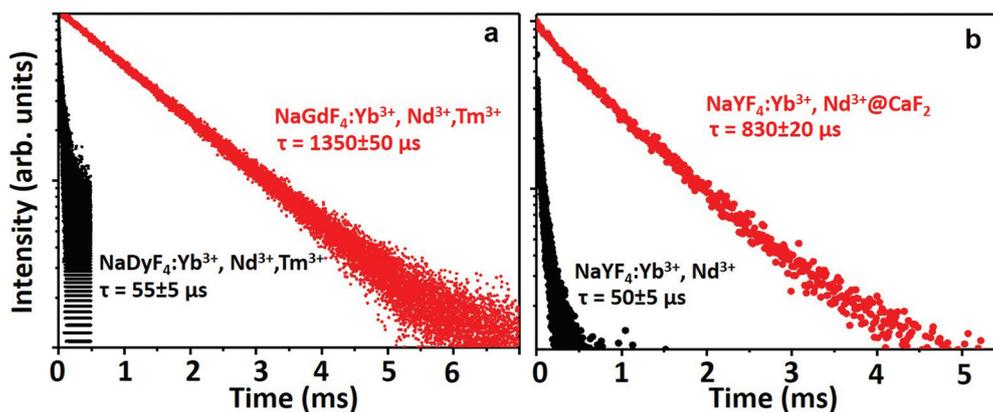
Fig. 3 Fluorescence decay curves of the emission observed at 1000 nm corresponding to: a. NaGdF$_4$:2% Yb^{3+},3% Nd^{3+},0.2% Tm^{3+} NPs and NaDyF$_4$:2% Yb^{3+},3% Nd^{3+},0.2% Tm^{3+} NPs. b. PAA-coated NaYF$_4$:10% Yb^{3+},30% Nd^{3+}@CaF$_2$ core/shell NPs.

valent concentration of NPs in the aqueous dispersion (10 mg mL^{-1}), our optimized core/shell NPs present a much brighter emission signal than Ag$_2$S NPs. In addition, the short lifetime of Ag$_2$S NPs (tens of nanoseconds) does not allow their application in time-gated imaging, as is demonstrated in Fig. S15,† in which a delay time of 10 μs is enough to eliminate the fluorescence signal generated by Ag$_2$S NPs. The absolute quantum yield of our core/shell NPs was estimated to be ~11 ± 1% using an integrating sphere method, which is much higher than the emission quantum yield of Ag$_2$S of 0.15–4.7%.[64,65] This is in agreement with the observed comparison of emission brightness.

Their excellent optical properties led us to test both types of NPs for autofluorescence-free time-gated imaging. In particular, NaGdF$_4$:2% Yb^{3+},3% Nd^{3+},0.2% Tm^{3+} NPs were tested for real-time tracking of the distribution of NPs after an oral administration of 200 μL of a 4 mg mL^{-1} dispersion of NPs in water. To test the NPs under the most adverse conditions, C57BL/6 mice were used, as they present a very intense autofluorescence due to the skin pigmentation.[13] This can be seen in Fig. 4a, which shows the ventral fluorescence image of a mouse immediately after NP administration and without applying any delay. The strong autofluorescence caused by the skin pigmentation of the animal is clearly observed, together
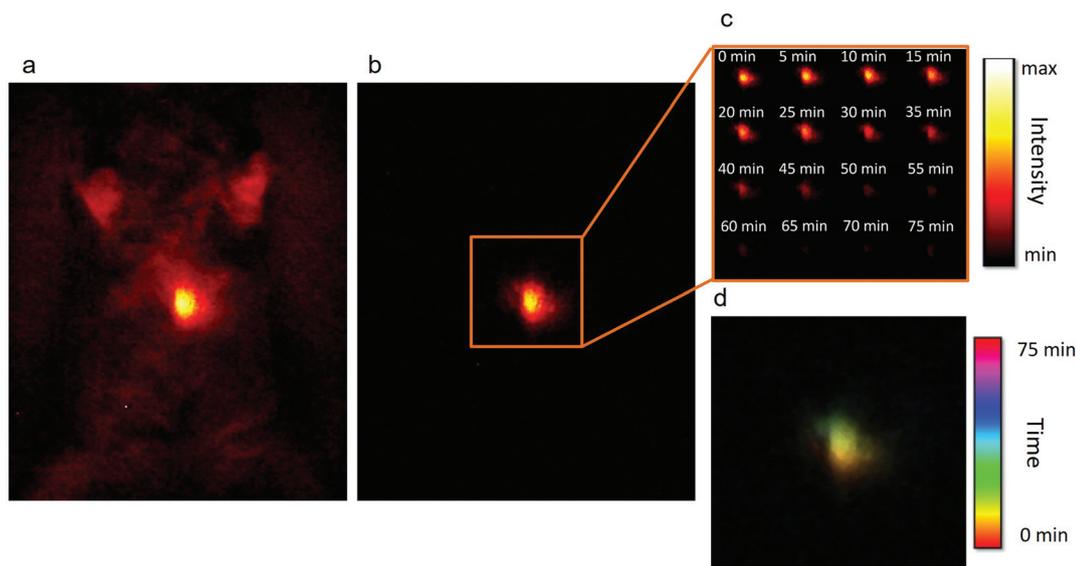

Fig. 4 a. Fluorescence ventral image of a black CD1 mouse after oral administration of a dispersion of NaGdF$_4$:Yb^{3+},Nd^{3+},Tm^{3+} NPs in water. The image was taken without time delay so the autofluorescence of the mouse is clearly seen, especially from the region of the stomach. b. Image of the same animal after applying a delay time of 1 μs. Only the signal coming from the NPs can be observed. c. Intensity-based real-time tracking of the distribution of NPs in the stomach. The signal displaces towards the duodenum and the intensity decreases as the NPs get absorbed in the intestine. d. Time-lapse color-coded composition of the images shown in c, showing the position of the NPs in one color for each time. It can be seen that the NPs are initially located at the bottom of the stomach (reddish color) but in the final moments the NPs are mainly located close to the duodenum (greenish color).

with a strong signal coming from the abdomen, which can be attributed to the autofluorescence of the animal's diet and the liver. Once a delay of 1 μs is applied (Fig. 4b), the signal generated by the NPs can be easily localized and isolated from the autofluorescence signal. To obtain these images, only one accumulation with an integration time of 30 ms was required, which makes this system compatible with real-time NP tracking. In particular, we monitored the transit of the administered NPs from the stomach to the intestine, as shown in Fig. 4c and d. Two combined effects can be observed over time: first, as the NPs are deposited at the bottom of the stomach, the fluorescence signal displaces up and to the left, in the direction of the duodenum; and second, once the NPs have reached the exit of the stomach, the intensity decreases. This decrease in the intensity indicates the progressive transit of the NPs to the intestine. In the particular case shown in Fig. 4c, it took around 75 minutes for the majority of the NPs to exit the stomach. The lack of signals from the intestine indicates that the NPs are rapidly absorbed at the beginning of the tube. Fig. 4d shows a color-coded time-lapse image composed with the images shown in Fig. 4c. The images have been generated by overlapping the position of the maxima of fluorescence in a different color for each time. The figure indicates that the fluorescence signal is initially (reddish color) located at the bottom of the stomach, whereas later (greenish color) the NPs

are concentrated in an upper-left position, which matches the position of the valve that connects the stomach to the duodenum. The *ex vivo* study of the organs confirmed that most of the NPs had abandoned the stomach, as only a weak emission was registered in that organ, and that the NPs had been absorbed in the intestine, as no signal from the NPs could be observed (Fig. S16†). The importance of this study stems from the fact that the transit time of substances from the stomach to the intestine, and subsequently, to the bloodstream, depends on many factors that cannot be externally controlled (*e.g.* the amount of food present in the stomach or the level of activity of the animal can affect the speed of the process).[66,67] The transit rate, in turn, has a strong influence on the absorption of orally administered drugs as, among other reasons, it determines the concentration of the drug in the plasma and its bioavailability.[68] Our approach provides a powerful alternative to the models and simulations that are usually employed to study gastrointestinal transit,[67,69] because it allows real time tracking of the NP distribution thanks to their fluorescence.

A different set of experiments, also designed for their potential of autofluorescence-free *in vivo* imaging, was performed with the NaYF$_4$:10% Yb^{3+},30% Nd^{3+}@CaF$_2$ NPs. In this case, the core/shell NPs were first used for *in vivo* autofluorescence-free time-gated imaging. In our experiment, we compared the NIR fluorescence images obtained for a C57BL/
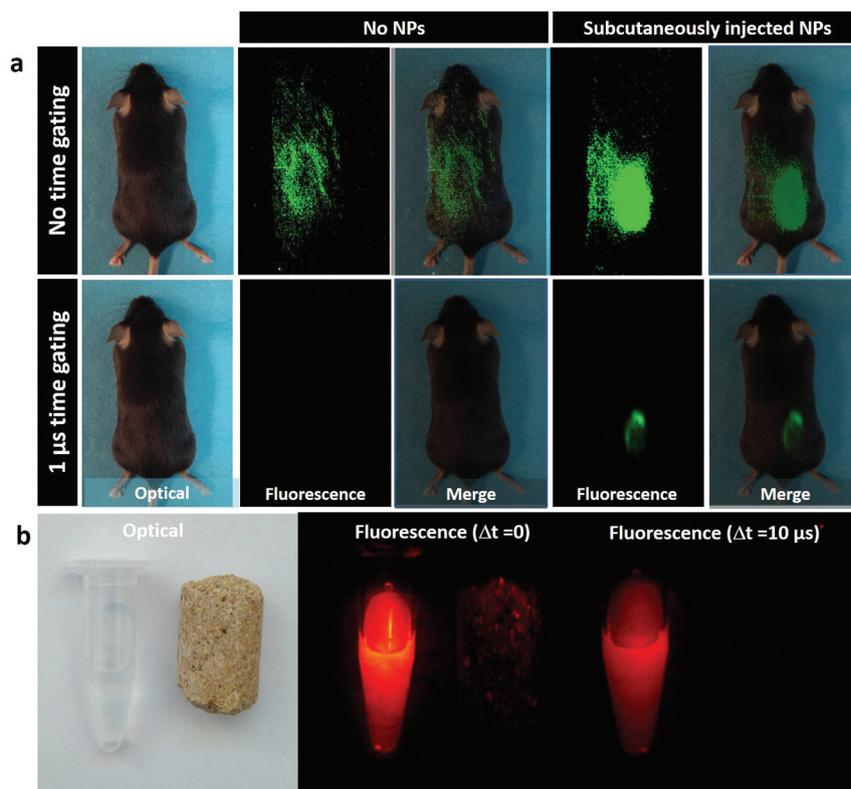

Fig. 5   a. Optical and NIR (900−1700 nm) images of C57/Bl6 mice, one of them injected with 50 μl NaYF$_4$:10% Yb^{3+},30% Nd^{3+}@CaF$_2$ NPs and the other acting as a control. Fluorescence images were recorded for no delay and for a 1 μs delay time. b. NIR images of NaYF$_4$:10% Yb^{3+},30% Nd^{3+}@CaF$_2$ dispersion and feedstuff detected with zero and 10 μs time delay.
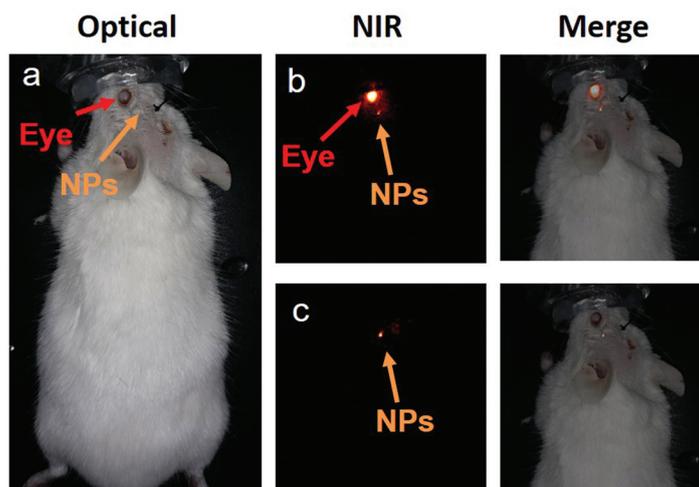
Fig. 6 a. Optical image of a CD1 mouse after intracerebral injection of $NaYF_4$: 10% Yb^{3+},30% Nd^{3+}@CaF_2 NPs. b. NIR fluorescence image of the mouse in (a) as obtained with no time delay between excitation pulse and image collection. The merge between optical and fluorescence images is shown to indicate that the brightest fluorescence emission corresponds to eye autofluorescence. c. NIR time-gated fluorescence image, as obtained for the mouse in (a) when a 1 μs time delay is introduced between excitation and image collection. The merged images show that the autofluorescence generated by the eye was successfully removed.

6 mouse subcutaneously injected with our core/shell NPs and a control mouse (to which no NPs were administered) when no delay between laser pulse and image collection was applied and when a 1 μs delay time was applied (Fig. 5a). In the absence of any time delay, a strong background of autofluorescence is evidenced in both control and injected mice. Indeed, the autofluorescence-related background is so strong that it is difficult to elucidate the position of the injection, whereas an introduction of a time delay leads to a complete removal of the autofluorescence background, making it possible to trace clearly the location of the subcutaneous NP injection in the mouse. These images unmistakably indicate the capability of time-gated imaging for complete elimination of the autofluorescence background in the NIR. This is useful not only to avoid skin autofluorescence, but also to avoid undesirable organ autofluorescence, which can be affected by animal diet. In Fig. 5b, it is shown that the NIR emission signal generated by a food pellet can be successfully removed using time-gated imaging. When no decay is established, the foodstuff displays a weak but non-negligible emission signal, which disappears when time-gated imaging is applied.

Then, the core/shell NPs were used for transcranial fluorescence imaging. To do so, the core/shell NPs were directly injected into a CD1 mouse brain, as indicated in Fig. 6a. The mouse was injected intracerebrally with 100 nL of a dispersion of $NaYF_4$:10% Yb^{3+},30% Nd^{3+}@CaF_2 NPs. The extremely low volume of NPs that can be injected into the brain to avoid adverse effects makes it of paramount importance to increase the contrast of the image by eliminating any nonspecific background such as that generated by autofluorescence of the eyes. In particular, when dealing with head and brain imaging, the NIR fluorescence signal is hindered by the autofluorescence emission of the eyes in both NIR I and NIR II windows, which

can be attributed to the presence of melanin. This is evidenced in Fig. 6b, where the NIR image (obtained under continuous wave 808 nm excitation) of a mouse with an intracranial injection of our infrared emitting core/shell NPs is shown. As shown in Fig. 6c, the autofluorescence emission at the eye can be completely eliminated by performing time-gated imaging with a time delay of 1 μs, allowing for a straightforward localization of the NPs inside the brain. As was the case for orally administrated NPs, the image shown in Fig. 6b corresponds to a single accumulation with a 30 ms integration time. This indicates the adequacy of our strategy for performing autofluorescence-free real time monitoring of brain structures and processes even at very low NP amounts. The results included in Fig. 6 open the way for the use of rare-earth-doped NPs for brain imaging as the basis of advanced cerebral studies.

4. Conclusion

In conclusion, we have developed two different approaches for obtaining NPs with intense luminescence and long fluorescence lifetime in NIR II. First, the effect of the selection of dopants to optimize the energy transfer processes and the obtained $NaGdF_4$:2% Yb^{3+},3% Nd^{3+},0.2% Tm^{3+} NPs (~13 nm) with a bright emission at 980 nm and a lifetime of 1.3 ms was explored. Second, we synthesized sub-10 nm monodisperse core/shell $NaYF_4$:10% Yb^{3+},30% Nd^{3+}@CaF_2 NPs with high dopant concentrations, which show a strong NIR II emission at 1000 nm with a long lifetime close to 1 millisecond. The advantages of core/shell engineering and selective doping were systematically investigated, allowing for a fine optimization of the fluorescence properties. The possibility of efficient optical excitation in NIR I and bright emission in NIR II with fluo-

rescence decay times around 1 millisecond (orders of magnitude longer than that of tissue autofluorescence) makes our NPs superior candidates for high penetration, autofluorescence-free *in vivo* NIR imaging using a time-gated approach. This was experimentally demonstrated through the performance of simple but conclusive *in vivo* experiments in murine models: real-time tracking of gastrointestinal absorption of orally administered NPs and transcranial autofluorescence-free imaging of intracerebrally injected NPs. This fact, coupled with their outstanding brightness, which surpasses that of commonly used NIR-emitting Ag_2S nanoparticles, makes our NPs great candidates as contrast agents for high-contrast deep tissue bioimaging in the time domain.

Conflicts of interest

There are no conflicts to declare.

Acknowledgements

References

1 F. Leblond, S. C. Davis, P. A. Valdés and B. W. Pogue, *J. Photochem. Photobiol., B*, 2010, **98**, 77–94.
2 C.-H. Quek and K. W. Leong, *Nanomaterials*, 2012, **2**, 92–112.
3 K.-T. Yong, Y. Wang, I. Roy, H. Rui, M. T. Swihart, W.-C. Law, S. K. Kwak, L. Ye, J. Liu and S. D. Mahajan, *Theranostics*, 2012, **2**, 681.
4 M. Sauer and M. Heilemann, *Chem. Rev.*, 2017, **117**, 7478–7509.
5 B. Huang, W. Q. Wang, M. Bates and X. W. Zhuang, *Science*, 2008, **319**, 810–813.
6 S. Andersson-Engels, C. af Klinteberg, K. Svanberg and S. Svanberg, *Phys. Med. Biol.*, 1997, **42**, 815.
7 Q. T. Nguyen, E. S. Olson, T. A. Aguilera, T. Jiang, M. Scadeng, L. G. Ellies and R. Y. Tsien, *Proc. Natl. Acad. Sci. U. S. A.*, 2010, **107**, 4317–4322.
8 S. Gioux, H. S. Choi and J. V. Frangioni, *Mol. Imaging*, 2010, **9**, 237.
9 A. L. Vahrmeijer, M. Hutteman, J. R. van der Vorst, C. J. H. van de Velde and J. V. Frangioni, *Nat. Rev. Clin. Oncol.*, 2013, **10**, 507–518.
10 J. V. Frangioni, *Curr. Opin. Chem. Biol.*, 2003, **7**, 626–634.
11 E. A. Cowles, J. L. Kovar, E. T. Curtis, H. Xu and S. F. Othman, *BioRes. Open Access*, 2013, **2**, 186–191.
12 A. P. Patterson, S. A. Booth and R. Saba, *BioMed Res. Int.*, 2014, **2014**, 1–14.
13 B. del Rosal, I. Villa, D. Jaque and F. Sanz-Rodríguez, *J. Biophotonics*, 2016, **9**, 1059–1067.
14 A. M. Smith, M. C. Mancini and S. Nie, *Nat. Nanotechnol.*, 2009, **4**, 710–711.
15 G. S. Hong, S. Diao, J. L. Chang, A. L. Antaris, C. X. Chen, B. Zhang, S. Zhao, D. N. Atochin, P. L. Huang, K. I. Andreasson, C. J. Kuo and H. J. Dai, *Nat. Photonics*, 2014, **8**, 723–730.
16 G. Hong, J. T. Robinson, Y. Zhang, S. Diao, A. L. Antaris, Q. Wang and H. Dai, *Angew. Chem.*, 2012, **51**, 9818–9821.
17 A. N. Bashkatov, E. A. Genina, V. I. Kochubey and V. V. Tuchin, *J. Phys. D: Appl. Phys.*, 2005, **38**, 2543.
18 J. T. Robinson, G. Hong, Y. Liang, B. Zhang, O. K. Yaghi and H. Dai, *J. Am. Chem. Soc.*, 2012, **134**, 10664–10669.
19 D. J. Naczynski, M. C. Tan, M. Zevon, B. Wall, J. Kohl, A. Kulesa, S. Chen, C. M. Roth, R. E. Riman and P. V. Moghe, *Nat. Commun.*, 2013, **4**, 2199–2199.
20 C. Caltagirone, A. Bettoschi, A. Garau and R. Montis, *Chem. Soc. Rev.*, 2015, **44**, 4645–4671.
21 G. Hong, J. T. Robinson, Y. Zhang, S. Diao, A. L. Antaris, Q. Wang and H. Dai, *Angew. Chem., Int. Ed.*, 2012, **51**, 9818–9821.
22 A. Benayas, F. Ren, E. Carrasco, V. Marzal, B. del Rosal, B. A. Gonfa, Á. Juarranz, F. Sanz-Rodríguez, D. Jaque and J. García-Solé, *Adv. Funct. Mater.*, 2015, **25**, 6650–6659.
23 C. Li, Y. Zhang, M. Wang, Y. Zhang, G. Chen, L. Li, D. Wu and Q. Wang, *Biomaterials*, 2014, **35**, 393–400.
24 Y. Zhang, G. Hong, Y. Zhang, G. Chen, F. Li, H. Dai and Q. Wang, *ACS Nano*, 2012, **6**, 3695–3702.
25 L. Gu, D. J. Hall, Z. Qin, E. Anglin, J. Joo, D. J. Mooney, S. B. Howell and M. J. Sailor, *Nat. Commun.*, 2013, **4**, 2326.
26 H. Osaki, C. M. Chou, M. Taki, K. Welke, D. Yokogawa, S. Irle, Y. Sato, T. Higashiyama, S. Saito and A. Fukazawa, *Angew. Chem., Int. Ed.*, 2016, **128**, 7247–7251.
27 D. Jin, J. A. Piper and A. Chem, *Anal. Chem.*, 2011, **83**, 2294–2300.
28 X. Zheng, X. Zhu, Y. Lu, J. Zhao, W. Feng, G. Jia, F. Wang, F. Li and D. Jin, *Anal. Chem.*, 2016, **88**, 3449–3454.
29 L. Gu, D. J. Hall, Z. Qin, E. Anglin, J. Joo, D. J. Mooney, S. B. Howell and M. J. Sailor, *Nat. Commun.*, 2013, **4**, 2326–2326.
30 M. Rajendran and L. W. Miller, *Biophys. J.*, 2015, **109**, 240–248.

31 J. Joo, X. Liu, V. R. Kotamraju, E. Ruoslahti, Y. Nam and M. J. Sailor, *ACS Nano*, 2015, **9**, 6233.

32 W. T. Carnall, P. R. Fields and K. Rajnak, *J. Chem. Phys.*, 1968, **49**, 4424–4442.

33 J. C. G. Bünzli and C. Piguet, *Chem. Soc. Rev.*, 2005, **34**, 1048–1077.

34 R. Wang, X. Li, L. Zhou and F. Zhang, *Angew. Chem., Int. Ed.*, 2014, **53**, 12086–12090.

35 E. S. Levy, C. A. Tajon, T. S. Bischof, J. Iafrati, A. Fernandezbravo, D. J. Garfield, M. Chamanzar, M. M. Maharbiz, V. S. Sohal and P. J. Schuck, *ACS Nano*, 2016, **10**, 8423–8433.

36 L. Ma, Y. Liu, L. Liu, A. Jiang, F. Mao, D. Liu, L. Wang and J. Zhou, *Adv. Funct. Mater.*, 2017, 1705057.

37 B. del Rosal, D. H. Ortgies, N. Fernández, F. Sanz-Rodríguez, D. Jaque and E. M. Rodríguez, *Adv. Mater.*, 2016, **28**, 10188–10193.

38 D. J. Naczynski, M. C. Tan, M. Zevon, B. Wall, J. Kohl, A. Kulesa, S. Chen, C. M. Roth, R. E. Riman and P. V. Moghe, *Nat. Commun.*, 2013, **4**, 1345–1346.

39 Y. Zhong, Z. Ma, S. Zhu, J. Yue, M. Zhang, A. L. Antaris, J. Yuan, R. Cui, H. Wan and Y. Zhou, *Nat. Commun.*, 2017, **8**, 737.

40 W. Shao, G. Chen, A. Kuzmin, H. L. Kutscher, A. Pliss, T. Y. Ohulchanskyy and P. N. Prasad, *J. Am. Chem. Soc.*, 2016, **138**, 16192.

41 M. Kamimura, N. Kanayama, K. Tokuzen, K. Soga and Y. Nagasaki, *Nanoscale*, 2011, **3**, 3705–3713.

42 H. Dong, L. D. Sun and C. H. Yan, *Chem. Soc. Rev.*, 2015, **44**, 1608–1634.

43 Y. F. Wang, G. Y. Liu, L. D. Sun, J. W. Xiao, J. C. Zhou and C. H. Yan, *ACS Nano*, 2013, **7**, 7200–7206.

44 A. Brenier, *J. Opt. Soc. Am. B*, 2006, **23**, 2209–2216.

45 L. Tu, X. Liu, F. Wu and H. Zhang, *Chem. Soc. Rev.*, 2015, **44**, 1331–1345.

46 Y. Jeong, J. Sahu, D. Payne and J. Nilsson, *Opt. Express*, 2004, **12**, 6088–6092.

47 W. F. Krupke, *IEEE J. Sel. Top. Quantum Electron.*, 2002, **6**, 1287–1296.

48 J. Shen, G. Chen, A. M. Vu, W. Fan, O. S. Bilsel, C. C. Chang and G. Han, *Adv. Opt. Mater.*, 2014, **1**, 644–650.

49 Y. T. Zhong, G. Tian, Z. Gu, Y. J. Yang, L. Gu, Y. L. Zhao, Y. Ma and J. N. Yao, *Adv. Mater.*, 2014, **26**, 2831–2837.

50 H. Wen, H. Zhu, X. Chen, T. F. Hung, B. Wang, G. Zhu, S. F. Yu and F. Wang, *Angew. Chem.*, 2013, **52**, 13419–13423.

51 X. Xie, N. Gao, R. Deng, S. Qiang, Q. H. Xu and X. Liu, *J. Am. Chem. Soc.*, 2013, **135**, 12608–12611.

52 X. Zhang, Z. Zhao, X. Zhang, D. B. Cordes, B. Weeks, B. Qiu, K. Madanan, D. Sardar and J. Chaudhuri, *Nano Res.*, 2015, **8**, 636–648.

53 N. J. Johnson, S. He, S. Diao, E. M. Chan, H. Dai and A. Almutairi, *J. Am. Chem. Soc.*, 2017, **139**, 3275–3282.

54 G. Y. Chen, J. Shen, T. Y. Ohulchanskyy, N. J. Patel, A. Kutikov, Z. P. Li, J. Song, R. K. Pandey, H. Agren, P. N. Prasad and G. Han, *ACS Nano*, 2012, **6**, 8280–8287.

55 K. Prorok, M. Pawlyta, W. Stręk and A. Bednarkiewicz, *Chem. Mater.*, 2016, **28**, 2295–2300.

56 L. Wang, H. Dong, Y. Li, R. Liu, Y. F. Wang, H. K. Bisoyi, L. D. Sun, C. H. Yan and Q. Li, *Adv. Mater.*, 2015, **27**, 2065.

57 Y. F. Wang, L. D. Sun, J. W. Xiao, W. Feng, J. C. Zhou, J. Shen and C. H. Yan, *Chemistry*, 2012, **18**, 5558.

58 N. J. J. Johnson, H. Sha, S. Diao, E. M. Chan, H. Dai and A. Almutairi, *J. Am. Chem. Soc.*, 2017, **139**, 3275.

59 D. Jaque, M. O. Ramirez, L. E. Bausá, J. G. Solé, E. Cavalli, A. Speghini and M. Bettinelli, *Phys. Rev. B: Condens. Matter Mater. Phys.*, 2003, **68**, 035118.

60 A. C. Berends, F. T. Rabouw, F. C. M. Spoor, E. Bladt, F. C. Grozema, A. J. Houtepen, L. D. A. Siebbeles and C. de Mello Donegá, *J. Phys. Chem. Lett.*, 2016, **7**, 3503–3509.

61 R. Arppe, I. Hyppanen, N. Perala, R. Peltomaa, M. Kaiser, C. Wurth, S. Christ, U. Resch-Genger, M. Schaferling and T. Soukka, *Nanoscale*, 2015, **7**, 11746–11757.

62 X. Zhang, Y. Gu and H. Chen, *J. Innovative Opt. Health Sci.*, 2014, **7**, 1350059.

63 X. Jia, D. Li, J. Li and E. Wang, *RSC Adv.*, 2015, **5**, 80929–80932.

64 G. Jingwen, W. Chuanli, D. Dan, W. Ping and C. Chenxin, *Adv. Healthcare Mater.*, 2016, **5**, 2437–2449.

65 D. H. Zhao, J. Yang, R. X. Xia, M. H. Yao, R. M. Jin, Y. D. Zhao and B. Liu, *Chem. Commun.*, 2018, **54**, 527.

66 M. Rowland, C. Peck and G. Tucker, *Annu. Rev. Pharmacol. Toxicol.*, 2011, **51**, 45–73.

67 A. Y. Abuhelwa, D. B. Williams, R. N. Upton and D. J. R. Foster, *Eur. J. Pharm. Biopharm.*, 2017, **112**, 234–248.

68 T. Kimura and K. Higaki, *Biol. Pharm. Bull.*, 2002, **25**, 149–164.

69 W. Huang, S. L. Lee and L. X. Yu, *AAPS J.*, 2009, **11**, 217–224.